Chinese Chemical Letters 34 (2023) 108397

Contents lists available at ScienceDirect

Chinese Chemical Letters

journal homepage: www.elsevier.com/locate/cclet

Elevated degradation of di-*n*–butyl phthalate by activating peroxymonosulfate over GO–$CoFe_2O_4$ composites: Synergistic effects and mechanisms

Qingliang Liu, Hang Qie, Zhiqiang Sun, Yufei Zhen, Liying Wu, Ying Zhao*, Jun Ma

State Key Laboratory of Urban Water Resource and Environment, Harbin Institute of Technology, Harbin 150090, China

ARTICLE INFO

Article history:
Received 10 November 2022
Revised 3 March 2023
Accepted 28 March 2023
Available online 31 March 2023

Keywords:
Peroxymonosulfate
Cobalt ferrite
Graphene oxide
Synergistic effect
Di-*n*–butyl phthalate

ABSTRACT

Rational design of heterogeneous catalysts with high activity and stability is crucial in peroxymonosulfate (PMS)-based oxidation treatment of wastewater. Herein, the graphite oxide-cobalt ferrite (GO-$CoFe_2O_4$) composite was constructed, and its morphological, component and structural characteristics were thoroughly examined, respectively. GO-$CoFe_2O_4$ obviously boosted PMS catalytic performance on di-*n*–butyl phthalate removal (DBP, $R_{DBP} = 90\%$, $R_{TOC} = 37\%$), which indicated by the first-order kinetic constant ($k_{DBP} = 0.060\ min^{-1}$) being roughly 4 times than pure $CoFe_2O_4$ ($k_{DBP} = 0.015\ min^{-1}$). The fabrication of GO-$CoFe_2O_4$ brought the favorable stability and repeatability up to six cycles. Moreover, the method of batch dosing catalyst was creatively proposed to improve the PMS utilization efficiency. The coupling of GO enhanced the dispersion of $CoFe_2O_4$ particles to obtain sufficient active sites, additionally, the plentiful C=O groups and free-flowing electrons on GO promoted GO-$CoFe_2O_4$ to coordinate a redox process during PMS activation. With the aid of theoretical calculations, GO-$CoFe_2O_4$ was revealed to exhibit a strong affinity toward PMS adsorption, where PMS spontaneously dissociated into sulfate radical ($SO_4^{\bullet-}$), hydroxyl radical ($^{\bullet}OH$) and singlet oxygen ($^1O_2$), acting as the reactive oxygen species (ROSs). Electrons cycling between Co, Fe and O species ensured continuous ROSs generation and excellent catalytic performance.

Di-*n*–butyl phthalate (DBP), a typical kind of phthalate esters, has been considered a priority controlled hazardous contaminant by U.S. EPA. It occurs at low concentrations in aquatic environments and poses considerable risk of endocrine-disrupting effects and metabolic disorders to human beings [1,2]. Moreover, the biodegradation kinetics of DBP are very slow in the natural environment, from dozens of days to more than 20 years [3]. Presently, the typical treatments, including adsorption, membrane separation, biodegradation as well as chemical oxidation, suffer from different drawbacks with regard to their remedy time scale and large energy consumption [4]. Consequently, it is highly demanded to explore a cost-efficient strategy for eliminating trace-level DBP.

Sulfate radical ($SO_4^{\bullet-}$)-based advanced oxidation processes (SR-AOPs) exhibit a favorable standard reduction potential (2.5–3.1 V *vs.* NHE), wide pH adaptability (2.0–9.0), longer half-life with regard to the hydroxyl radical (30–40 μs *vs.* 20 ns) and high oxidation selectivity [5]. These make it possible to employ SR-AOPs to decompose a variety of organic substances in sewage. $SO_4^{\bullet-}$ can be effectively generated by activating peroxymonosulfate (PMS) in conjunction with ultrasound, photolysis, heat, homogenous or heterogeneous catalysts [6]. Cobalt-based catalysts have been investigated, and it has been discovered that they are the most effective activators for cleaving the O–O bond in an asymmetric PMS structure [7]. Cobalt ferrite ($CoFe_2O_4$) belonging to the spinel-type ferrites family (S.G. Fd-3m) has indicated high activity and magnetic properties with excellent stability in order to degrade persistent pollutants [8]. The coupling effect between Co and Fe species might be more effective as a catalyst in PMS activation than their single component equivalent. Simultaneously, $CoFe_2O_4$ is characterized to have a high abundance of oxygen vacancies and surface hydroxyl groups, which also help to further activate PMS [9]. Ren *et al.* evaluated the performance of MFe_2O_4 (M = Co, Cu, Mn, Zn) in PMS activation, and concluded that $CoFe_2O_4$ showed higher catalytic activity toward PMS for the degradation of DBP, and all catalysts displayed excellent recycling and stability in the repeated batch experiment [10]. Nonetheless, the unprotected $CoFe_2O_4$ primary nanoparticles are prone to agglomeration, as a result, there are fewer active sites that are accessible and there is less dispersion in the reaction solution, which further reduces the effective-

* Corresponding author.
E-mail address: yzhao16@hit.edu.cn (Y. Zhao).

https://doi.org/10.1016/j.cclet.2023.108397
1001-8417/

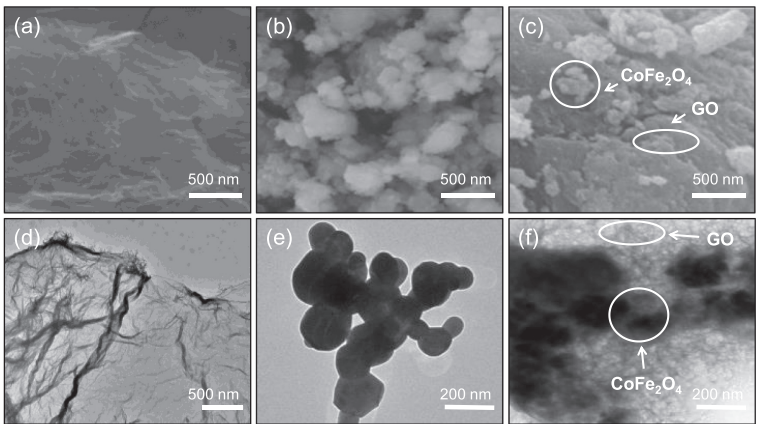

Fig. 1. SEM and TEM images of (a, d) GO, (b, e) $CoFe_2O_4$ and (c, f) 5%GO-$CoFe_2O_4$.

ness of PMS activation and organics decomposition [11]. Therefore, it is necessary to disperse $CoFe_2O_4$ on supporters for stable and efficient catalytic performance.

Recently, carbon-based materials were used to supporters for transition metal-based catalysts to fabricate carbon-loaded metal composites. Two-dimensional graphene oxide (GO) is a substance with various excellent properties of unique mechanical strength, high electrical conductivity and large specific surface area [12]. Multiple oxygen-containing functional groups including hydroxyl, carboxyl and epoxy situate at the basal plane and the edges of GO [13]. Metal components can be immobilized by such surface functionalization to create a solid structure and promote the separation and dispersion of spinel ferrite particles [14]. Furthermore, GO consists of the hexagonal ring-based carbon network with both sp^2- and sp^3-hybridized carbon atoms, the free-flowing unpaired electrons from the sp^2-hybridized carbon network promote electron transport between particles, further enhancing the catalytic PMS efficiency [15]. These specific surfaces structure of GO make it stand out as a suitable supporter [16]. Although, GO has been used to couple with some metal oxides such as Fe_2O_3, TiO_2, CoO_x, CoFeNi LDH, and even spinel ferrite [17–20]. However, rarely has the combination of GO and $CoFe_2O_4$ been reported for heterogeneous catalytic PMS. Particularly, the improving mechanism of GO-$CoFe_2O_4$ composites on catalytic PMS needs to be investigated, with a focus on the function of GO and the interaction between GO and $CoFe_2O_4$.

Herein, a series of GO-$CoFe_2O_4$ composites were fabricated and introduced to catalyze PMS for DBP removal. The degrading behavior and physicochemical properties were taken into consideration when choosing the optimized synthesis faction of catalyst. The impacts of different operational parameters, such as catalyst dosage, PMS concentration, initial DBP concentration and initial pH on the activity of GO-$CoFe_2O_4$/PMS system were systematically explored. The utilization efficiency of PMS was optimized by designing the GO-$CoFe_2O_4$ particles dosing process. Besides, the cycling stability performance of GO-$CoFe_2O_4$ was also examined. The radical quenching tests and ESR detection were conducted to determine the radicals produced by GO-$CoFe_2O_4$/PMS. Finally, the underlying enhanced mechanism of GO-$CoFe_2O_4$-catalyzed PMS was thoroughly clarified.

The detailed experimental methods were shown in Texts S1-S5 (Supporting information).

SEM and TEM techniques were utilized to witness the morphology of GO, $CoFe_2O_4$ and GO-$CoFe_2O_4$ (Fig. 1). Figs. 1a and d showed the multilayer GO structure with a slightly wrinkly surface. $CoFe_2O_4$ particles with diameters from 100 nm to 200 nm exhibited a rough and irregular polygonal shape and agglomerated appearance (Figs. 1b and e). For GO-$CoFe_2O_4$, it showed that the GO morphology was clear, and $CoFe_2O_4$ particles were well distributed on GO sheets (Figs. 1c and f). Besides, the support on GO sheets clearly suppressed the aggregation of $CoFe_2O_4$, which was attributed to the strong absorption between the multiple functional groups present on the surface of GO and metal sites [21]. It was beneficial to the heterogeneous PMS activation process.

Crystal structures of as-prepared materials were examined by XRD. As seen in Fig. S1 (Supporting information), as a precursor, GO had an intense diffraction peak at around $2\theta = 9.5°$, regarding the (001) interplanar distance of 0.76 nm, which represented that GO formed a well-ordered layered structure [22]. The pattern of $CoFe_2O_4$ in Fig. 2a exhibited peaks at 18.2°, 30.3°, 35.6°, 43.2°, 53.5°, 57.4° and 62.7° which were attributed to (111), (220), (311), (400), (422), (511) and (440) planes, respectively. These were in a well-defined crystal structure of spinel-type $CoFe_2O_4$ (JCPDS No. 22–1086, space group Fd 3m (227)). It was evident that the XRD pattern of GO-$CoFe_2O_4$ was basically consistent with pure $CoFe_2O_4$, without the typical diffraction peak of GO. It validated the successful deposition of $CoFe_2O_4$ between the inter-layers of GO. However, the introduction of GO increased the (311) intensity of $CoFe_2O_4$ obviously. It was due to the fact that a large number of -OH and -COOH groups on GO combined with H atoms of ferrite to strengthen the spinel structural properties of $CoFe_2O_4$ [23]. The peak intensity of GO-$CoFe_2O_4$ became low as the GO content increases to 10%. $CoFe_2O_4$ crystal growth was constrained by GO layers, and *in situ*-fabricated $CoFe_2O_4$ was covered by redundant GO layers [24].

The wide-scan XPS spectra demonstrated the co-existence of Co, Fe, O, C in 5%GO-$CoFe_2O_4$ composite (Fig. S2 in Supporting information). The EDS analysis in Fig. S3 (Supporting information) further confirmed the surface elemental composition of the $CoFe_2O_4$ and GO-$CoFe_2O_4$ material. The weight percentages of Co, Fe and O in $CoFe_2O_4$ were 31.48%, 56.75% and 10.35%, respectively (Table S1 in Supporting information). Another aspect, the weight percentages of Co, Fe, O and C in 5%GO-$CoFe_2O_4$ were 30.36%, 49.72%, 11.29% and 5.48%, respectively. The nominal loading weight percentage of GO and the fraction of C showed a strong correlation. Additionally, the less O component indicated the presence of oxygen defects on as-prepared materials.

According to Fig. 2b, FT-IR spectra of GO at about 1730, 1626, 1230 and 1031 cm^{-1} could ascribe to stretching vibration of C=O and C=C, O–H bending vibrations and C–O stretching vibrations, respectively [25]. Indeed, FT-IR spectra of pure $CoFe_2O_4$ displayed a peak at 564 cm^{-1}, which was attributed to the Co-O and Fe-O vibrations [26]. It was worth noting that in the spectra of GO-$CoFe_2O_4$, the peaks at 1730 and 1626 cm^{-1}, corresponding to the functional groups of C=O and C=C in GO, blue shifted.

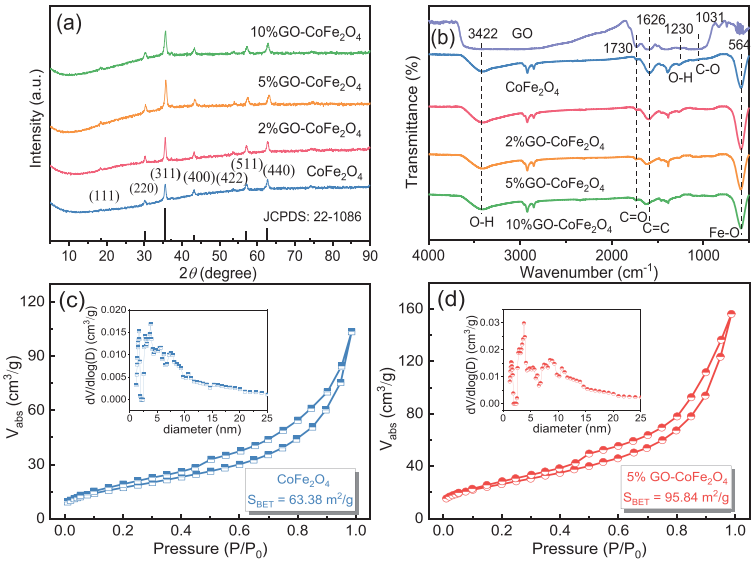

Fig. 2. (a) XRD patterns, (b) FT-IR spectra, (c, d) N_2 absorption-desorption isotherms of different catalysts, the inserts are the corresponding pore size distributions.

The Raman spectra of GO, $CoFe_2O_4$ and 5%GO-$CoFe_2O_4$ were depicted in Fig. S4 (Supporting information). At 1352 and 1584 cm^{-1}, respectively, two prominent Raman peaks matched with the D and G bands of GO were seen [27]. The degrees of defects and disorders of carbon materials could be clearly reflected by the intensity ratio of D band and G band. Since D and G's band intensities were fundamentally the same, graphitization of GO was to a lesser extent. It might be brought on the large number of groups that are present on its surface and cause considerable sp^3 hybridization. The D and G bands of GO were not found in Raman spectra of the composites because of the low concentration of GO in them. Additionally, $CoFe_2O_4$ and 5%GO-$CoFe_2O_4$ had obvious characteristic peaks at 323, 498 and 627 cm^{-1}, which were accountable for the stretching vibration of Fe-O on the tetrahedron [28].

The N_2 adsorption-desorption isotherms of $CoFe_2O_4$ and 5%GO-$CoFe_2O_4$ were given in Figs. 2c and d. As observed, both materials possessed the mesoporous structure due to the usual Langmuir-isotherm (type IV) with a hysteresis loop of H3-type and a centralized pore size distribution within 2–4 nm [29]. The related textural properties were summed up in Table S2 (Supporting information). The specific surface area of $CoFe_2O_4$ and 5%GO-$CoFe_2O_4$ was 63.38 and 95.84 m^2/g, respectively. This result confirmed our hypothesis that the GO sheets would act as a support and inhibit the aggregation of $CoFe_2O_4$ (as shown in Figs. 1c and f). Benefiting from the larger surface area, 5%GO-$CoFe_2O_4$ could expose more active sites and adequately contact with PMS and contaminations.

The catalytic performances of $CoFe_2O_4$ and GO-$CoFe_2O_4$ were determined for DBP removal *via* PMS activation. As presented in Fig. 3a, the individual PMS produced ~6% DBP elimination, indicating its negligible intrinsic oxidizing capacity. The GO/PMS system achieved 19% of DBP removal efficiency within 30 min, indicated that the PMS activation by GO had tiny contribution to DBP removal (Fig. S5 in Supporting information). However, with the addition of $CoFe_2O_4$, about 49% of DBP was removed within 30 min. Particularly, a significant increase in the catalytic properties could be effectively accomplished by GO loading, suggesting that the coupling effect between $CoFe_2O_4$ and GO greatly improved the activation capacity toward PMS. Meanwhile, the impact of GO content on the catalytic function of GO-$CoFe_2O_4$ was examined. The outcomes uncovered a positive correlation between the GO content and the catalytic performance of GO-$CoFe_2O_4$, however, the promotion effect was limited. For instance, 90% of DBP removal was obtained over 5%GO-$CoFe_2O_4$, while in the 10% GO-$CoFe_2O_4$/PMS system, 82% of DBP degradation was attained. The minimal DBP adsorption activity of all catalysts further demonstrated that the removal of DBP was due to degradation rather than adsorption (Figs. S5 and S6 in Supporting information). Additionally, the pseudo-first-order kinetics ($\ln(C/C_0) = -kt$) could fit the DBP degradation curves well. The rate constant (k_{DBP}) in 5%GO-$CoFe_2O_4$/PMS, which was 0.060 min^{-1} in Fig. 3b, was four times more than that in $CoFe_2O_4$/PMS, which was 0.015 min^{-1}. Moreover, 5%GO-$CoFe_2O_4$ exhibited better mineralization of DBP than $CoFe_2O_4$ (12% *vs.* 37% of TOC removal) in activating PMS. The results indicated that the heterogeneous structure instead of the physical mixing of GO and $CoFe_2O_4$ led to the enhanced catalytic function of GO-$CoFe_2O_4$.

Successive experiments were conducted to assess the potential for stability in the 5%GO-$CoFe_2O_4$/PMS catalytic system. As figuring out in Fig. 3c, 5%GO-$CoFe_2O_4$ continued to exhibit high catalytic activity in the sixth runs. A slight decline in DBP degradation efficiency might cause the unavoidable reduction of catalytic sites during recycling and cleaning. Then, ICP-OES analysis was used to look at the metal leaching capabilities of catalysts. Less than 0.05 and 0.02 mg/L of Co and Fe ions leaked after each cycle, respectively (Fig. 3d). Only around 3% of DBP was lost as a result of leaching, indicating the dominant role of heterogenous catalytic reaction on 5%GO-$CoFe_2O_4$. Therefore, it demonstrated excellent stability and recyclability for DBP elimination during PMS activation.

Considering the optimal performance of 5%GO-$CoFe_2O_4$ and its great potential for practical use, these variable parameters, such as catalyst dosage, initial DBP concentration, PMS concentration, initial pH and temperature were analyzed. The results were displayed in Fig. 4. In Fig. 4a, when the catalyst dosage was raised from 0.02 g/L to 0.2 g/L, DBP degradation was accelerated from 55% to 93%. The apparent improvement in DBP removal might be explained by a greater dosage of 5%GO-$CoFe_2O_4$, which could have created more surface-active sites that assisted in PMS activation and further led to the creation of more reactive ROS. While the DBP degradation minor decreased as the catalyst dosage was increased further, to 0.4 g/L. This finding might primarily be explained by the fact that extra more catalyst particles would self-bond to form aggregates, resulting in a less effective use of active sites on catalyst surfaces [30].

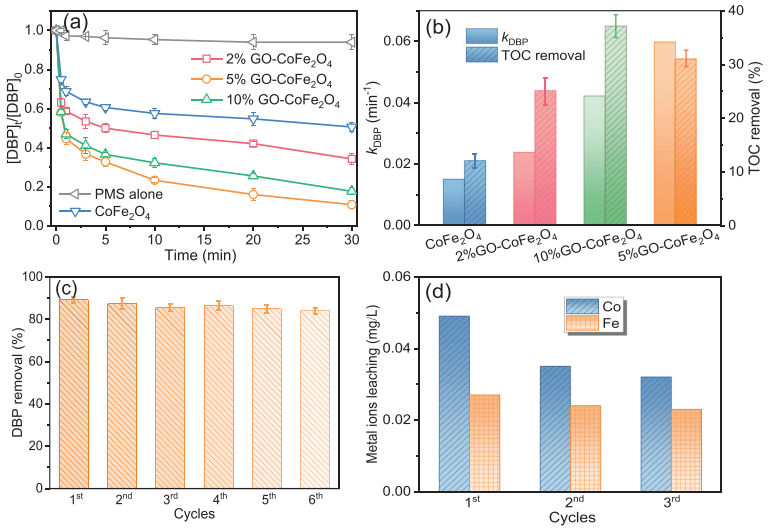

Fig. 3. (a) DBP removal and (b) *k* constants and TOC removal in different PMS oxidation systems. (c) Consecutive use of the catalytic activity of 5%GO-$CoFe_2O_4$. (d) The concentration of leaching metal ions for 5%GO-$CoFe_2O_4$. Catalysts: 0.1 g/L, $C_{0[DBP]}$: 2 μmol/L, $C_{[PMS]}$: 20 μmol/L, initial pH of 7.0, *T*: 20 ± 2 °C.

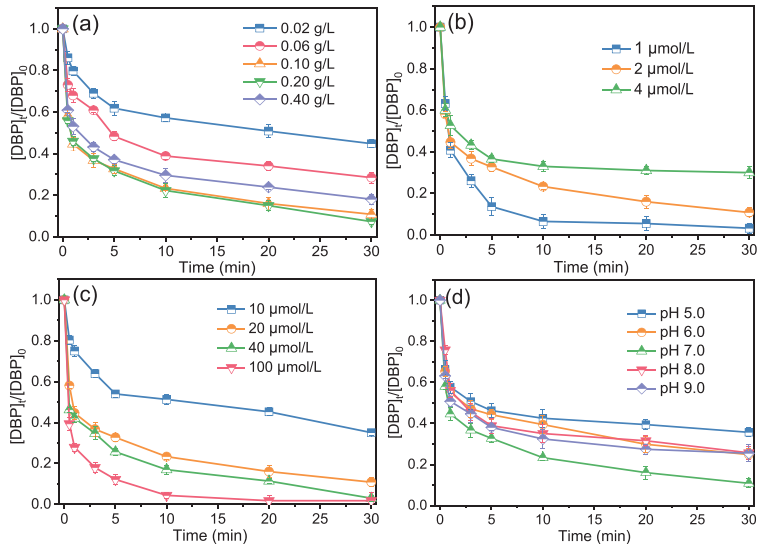

Fig. 4. Effect of (a) catalyst dosage, (b) initial DBP concentration, (c) PMS concentration and (d) initial pH on DBP degradation in the 5%GO-$CoFe_2O_4$/PMS system. Catalysts: 0.1 g/L, $C_{0[DBP]}$: 2 μmol/L, $C_{[PMS]}$: 20 μmol/L, initial pH of 7.0, *T*: 20 ± 2 °C.

The concentration of contaminants, as an essential component in the treatment of wastewater, had a significant influence on the quantity and duration of PMS that were required. Evidently, raising the initial concentration of DBP slowed down its degradation, as seen in Fig. 4b. As the DBP concentration rose from 1 μmol/L to 4 μmol/L, the DBP elimination in the 5%GO-$CoFe_2O_4$/PMS system fell from 97% to 70%. Higher initial concentrations caused less efficient DBP breakdown because more DBP molecules competed for the limited number of reactive species. Additionally, more pollutant molecules would bind to the surface of catalysts that prevented PMS from reacting with the redox-active centers of 5%GO-$CoFe_2O_4$. Therefore, an initial DBP concentration of 2 μmol/L was used in our tests to provide appropriate DBP removal and to mimic the trace level in real situations. Furthermore, PMS was an important source of ROSs (*i.e.*, $SO_4^{\bullet-}$, $^{\bullet}OH$, $^1O_2$) in the oxidation system, also playing a key role in the 5%GO-$CoFe_2O_4$/PMS system. DBP removal rate increased from 65% to 98% with PMS concentration ranging from 10 μmol/L to 100 μmol/L, as shown in Fig. 4c. The more PMS participated in the catalytic reaction to form ROSs to enhance the degradation of pollutants.

For the 5%GO-$CoFe_2O_4$/PMS system, the effect of initial solution pH on DBP removal was identified. As can be observed from Fig. 4d, DBP elimination significantly improved from 64% to 90% at initial pH values varying from 5.0 to 7.0. The effectiveness of DBP degradation decreased to 75% even though the solution pH climbed further to 9.0. It is widely established that the catalyst surface would become neutral, protonated, or deprotonated, respectively, depending on whether the solution pH was near to, below, or above the pH_{PZC} [31]. The surface of 5%GO-$CoFe_2O_4$ became deprotonated and negatively charged at pH > 6.8 (pH_{PZC}), which made HSO_5^- less likely to bind to the surface of catalyst owing to electrostatic repulsion. In addition, $SO_4^{\bullet-}$ would react with OH^- to generate $^{\bullet}OH$ with relatively weak oxidative capacity, making the inhibition of DBP removal. Whereas, the decreased removal efficacy of DBP in acidic circumstances was considered to be caused by the creation of an H-bond between H^+ and the O–O group of HSO_5^-, which led to the comparatively high stability of the oxidant [32].

The degradation efficiency of DBP with different amounts of humic acid (HA) or various anions in the 5%GO-$CoFe_2O_4$/PMS system

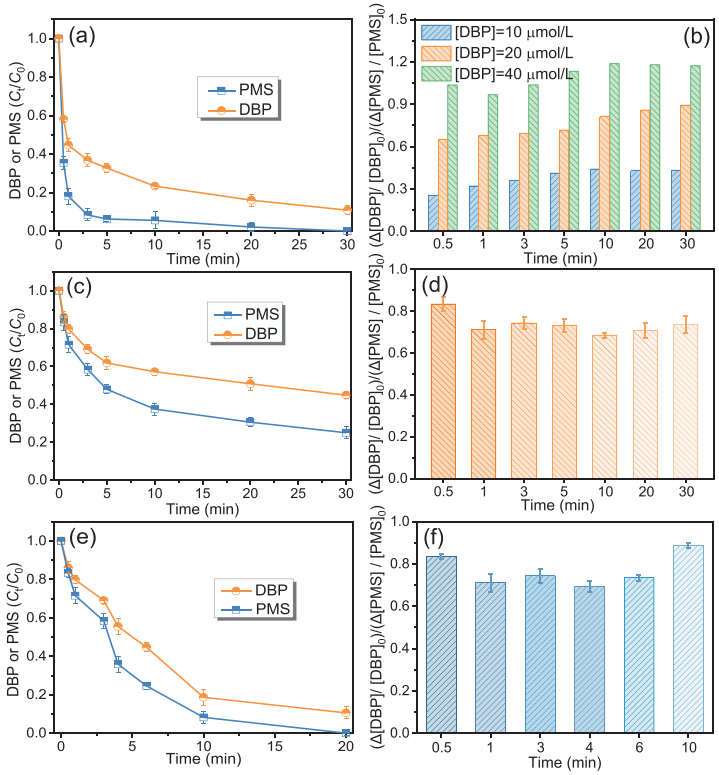

Fig. 5. (a) DBP removal and PMS decomposition in 5%GO-$CoFe_2O_4$/PMS. (b) Effect of DBP concentration on PMS utilization in 5%GO-$CoFe_2O_4$/PMS. Effect of (c, d) catalyst dosage and (e, f) catalyst dosing method on DBP removal, PMS decomposition and PMS utilization. Catalysts: 0.1 g/L (a, b, e, f) or 0.02 g/L (c, d), $C_{0[DBP]}$: 2 μmol/L (a, c-f), $C_{[PMS]}$: 20 μmol/L, initial pH of 7.0, T: 20 ± 2 °C.

was investigated (Fig. S7 in Supporting information). Almost no apparent inhibition on DBP removal efficiency could be observed in the presence of HA with the concentrations in the range of 0–10 mg/L. Besides, the common inorganic species (*e.g.*, Cl^-, HCO_3^-, and NO_3^- ions) with different concentrations also exhibited a very limited effect on DBP degradation. Herein, 5%GO-$CoFe_2O_4$ could be a promising heterogeneous catalyst in PMS activation for the degradation of organic pollutants [33,34].

The PMS decomposition was detected in the 5%GO-$CoFe_2O_4$/PMS system, its change trend was consistent with the DBP degradation (Fig. 5a). 91% of PMS was rapidly consumed in the first 3 min, indicating that PMS molecules were rapidly decomposed to generate large amounts of ROSs at this stage. PMS could not be detected at the end of the catalytic reaction. The reaction stoichiometric efficiency was further used to quantify the utilization efficiency of PMS for DBP degradation, it was defined as the ratio of the number of moles of DBP oxidized ($\Delta[DBP]/[DBP]_0$) to the number of moles of PMS consumed ($\Delta[PMS]/[PMS]_0$) in the presence of 5%GO-$CoFe_2O_4$ [35]. As shown in Fig. 5b, PMS utilization increased over reaction time ($U_{0.5} = 0.63$ to $U_{30} = 0.87$). Besides, with the increase of initial DBP concentration, PMS utilization showed an increasing trend. It was attributed to the fact that the produced amount of ROSs far exceeded the required amount of ROSs for DBP degradation in the initial stage of the reaction, so more DBP molecules could consume the excess ROSs, thereby improving the utilization of PMS. Unfortunately, increasing the initial DBP concentration improved the utilization of PMS, but decreased DBP removal rate. Additionally, we tried to reduce the catalyst dosage to 0.02 g/L, DBP degradation and PMS decomposition were 53.1% and 70%, respectively (Fig. 5c). PMS utilization remained around 0.7 (Fig. 5d). Apparently, although PMS was well utilized when increasing DBP concentration or decreasing catalyst dosage, DBP degradation was not satisfactory.

Considering the practical application, it is necessary to find a reasonable method to improve the PMS utilization efficiency while ensuring DBP degradation. In view of the above, a method, batch delivery of catalyst, was carried out. 0.01 g of catalyst was added to the system at reaction times of 0, 3, and 6 min, and PMS and DBP concentrations were determined. Such a dosing method made PMS always maintain at the stage of rapid decomposition. Therefore, PMS could sustainably generate ROSs to degrade DBP. DBP degradation efficiency reached 80% within 10 min and 90% after 20 min (Fig. 5e). On the other hand, PMS utilization was also maintained at a relatively high value ($U_{10} = 0.87$) (Fig. 5f). This dosing method not only saved the amount of catalyst and the reaction time but also achieved the desired degradation efficiency of substance.

DFT calculation was performed to investigate PMS adsorption characteristics and the cleavage of O–O bond on the (311) plane of $CoFe_2O_4$ and GO-$CoFe_2O_4$, respectively. As shown in Fig. 6, the atomic structures of a PMS molecule adsorbing on the surface of $CoFe_2O_4$ (311) (panel a) and GO-$CoFe_2O_4$ (100) (panel b) were established, respectively. As summarized in Table S3 (Supporting information), relative to a free PMS molecule without activation, the O–O bond length (l_{O-O}) of PMS was considerably lengthened after binding to catalysts. This implied an enhanced potential to break O–O bonds. The adsorption energy ($E_{ads}(HSO_5^-)$) of PMS on (311) plane of GO-$CoFe_2O_4$ was −3.14 eV, which was higher than the corresponding value for $CoFe_2O_4$ (311) ($E_{ads}(HSO_5^-) = -2.36$ eV), respectively. Moreover, the results of the bard charge analysis revealed that the PMS molecules and GO-$CoFe_2O_4$ experienced higher charge transfer ($Q = 0.16$ |e|). The stronger binding affinity and electron transferability indicated that the PMS bound on the GO-$CoFe_2O_4$ (311) was more active. It was in line with the conclusions of the experiments that GO-$CoFe_2O_4$ possessed better catalytic performance for PMS activation.

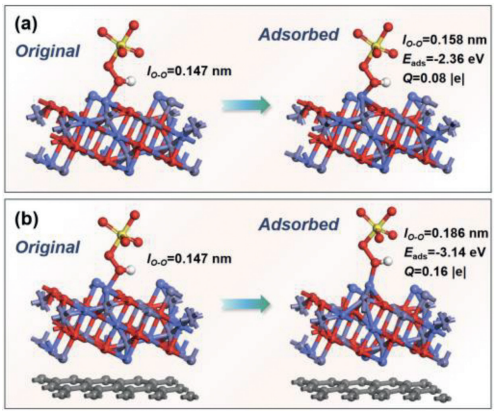

Fig. 6. The optimized crystal models of PMS adsorption on the (311) surface of (a) $CoFe_2O_4$ and (b) GO-$CoFe_2O_4$. The blue, purple, yellow, red, gray and white balls represent Co, Fe, S, O, C and H atoms, respectively.

In general, the generation efficiency of ROSs during PMS activation was mostly dictated by the catalysts' capacity to transport electrons. In order to highlight the synergy between GO and $CoFe_2O_4$ in GO-$CoFe_2O_4$ activating PMS, the electrochemical analysis was conducted to measure the redox potential and charge transfer ability in the of 0.5 mol/L Na_2SO_4 solution mixing with PMS. CV behaviors of $CoFe_2O_4$ and GO-$CoFe_2O_4$ were explored with a three-electrode device (Fig. 7a). Clear reduction currents were seen with the $CoFe_2O_4$ or GO-$CoFe_2O_4$ electrodes in the presence of PMS, proving that the reduction process took place on catalyst surfaces in tandem with the breakdown of PMS. Furthermore, GO-$CoFe_2O_4$ demonstrated a greater current density and superior reductive ability to $CoFe_2O_4$ for coordinating the redox process. It was proposed that GO-$CoFe_2O_4$ potentially exhibited a more reliable redox circulation than pure $CoFe_2O_4$, which made electron transfer possible in PMS activation.

Besides, to comprehend the charge transfer kinetics at the catalyst/solution interface, EIS plots of $CoFe_2O_4$ and GO-$CoFe_2O_4$ were recorded (Fig. 7b). Regarding to the EIS Nyquist plots, 5%GO-$CoFe_2O_4$ displayed the smallest semicircle diameter, which denoted the lowest charge transfer resistance. Accelerating the charge transfer during the catalytic decomposition of PMS proved advantageous. $CoFe_2O_4$ particles were dispersedly supported on GO to achieve the loose structure, and at the same time, the ability of electron transfer about $CoFe_2O_4$ particles was promoted by GO [36]. Therefore, the advantages of GO loading to $CoFe_2O_4$, which decreased $CoFe_2O_4$'s intrinsic charge transfer impedance and helped to improve the charge transport between GO-$CoFe_2O_4$, PMS, and DBP, were highlighted by the electrochemical results.

To examine the ROSs generated in the 5%GO-$CoFe_2O_4$/PMS system, quenching experiments were carried out (Fig. 8a). As a scavenger for $SO_4^{\bullet-}$ and $^{\bullet}OH$, methanol (MeOH) was utilized, with rate constants of 2.5×10^7 and 9.7×10^8 L mol^{-1} s^{-1}, respectively [37]. *tert*–Butyl alcohol (TBA), however, was thought to be the unique radical screening agent to selectively quenching $^{\bullet}OH$ (5.6×10^9 L mol^{-1} s^{-1}) [38]. The addition of 100 mmol/L TBA exhibited an obvious reduction of 42% on DBP degradation and the k_{DBP} value was decreased from 0.060 min^{-1} to 0.016 min^{-1} (Fig. 8b). It denoted that $^{\bullet}OH$ existed and help to remove DBP in such an oxidation system. A more noticeable negative impact on the clearance of DBP was seen after overdosing MeOH, the removal rate of DBP fell to 18%. The results had been validated that the results had been validated that the radical oxidation pathway ($SO_4^{\bullet-}$ and $^{\bullet}OH$) played a leading part in the oxidation of DBP due to almost complete suppression.

Besides, we employed superoxide dismutase (SOD, a typical $O_2^{\bullet-}$ quenching molecule) to quench the potential $O_2^{\bullet-}$ [39]. The negligible inhibition in degradation efficiency ruled out the involvement of $O_2^{\bullet-}$ in such a system. Additionally, after adding furfuryl alcohol (FFA, a classic $^1O_2$ scavenger) [40], DBP degradation was incredibly sluggish and 78% of DBP could be broken down. It was hypothesized that $^1O_2$ was generated and played a limited role in 5%GO-$CoFe_2O_4$/PMS. Therefore, these findings verified that the degrading mechanism for DBP during the 5%GO-$CoFe_2O_4$/PMS process primarily involved $SO_4^{\bullet-}$, $^{\bullet}OH$ and $^1O_2$, with the former two playing a major role.

To explicitly identify the relevant ROSs functioning in the GO-$CoFe_2O_4$/PMS catalytic process, *in situ* ESR studies were also conducted. The lack of distinctive peaks in the DMPO and PMS alone system, as shown in Fig. 8c, proved that no radical could be formed in the absence of catalysts. As anticipated, the $CoFe_2O_4$/PMS/DMPO system revealed a set of characteristic peaks indexed to DMPO-OH and DMPO-SO_4 adducts, certificating the production of $^{\bullet}OH$ and $SO_4^{\bullet-}$ radicals from the broken of peroxide O–O bond in PMS by $CoFe_2O_4$ [41]. The three-line peaks of the TEMP-$^1O_2$ adducts were simultaneously visible in the $CoFe_2O_4$/PMS/TEMP system with equal intensities, demonstrating the formation of $^1O_2$ (Fig. 8d) [42]. Notably, the inclusion of 5%GO-$CoFe_2O_4$ greatly increased the relative intensity of the ESR signals, indicating the formation of $^{\bullet}OH$, $SO_4^{\bullet-}$ and $^1O_2$ was enhanced by GO substrate in 5%GO-$CoFe_2O_4$/PMS.

Moreover, LSV analysis in Fig. S8a (Supporting information) was used to check the electron transfer pathway. The result demonstrated that the current density upon PMS addition followed by DBP addition showed negligible changes, which eliminated the occurrence of electron transfer pathways in the 5%GO-$CoFe_2O_4$/PMS system. The contribution of high-valence metal-oxo species for DBP degradation in the 5%GO-$CoFe_2O_4$/PMS system was also excluded by insignificantly adverse effects of DMSO in quenching experiment (Fig. S8b in Supporting information).

To gain knowledge about the catalytic process of 5%GO-$CoFe_2O_4$/PMS, the XPS spectra was employed. Significant alterations were seen through comparing the XPS spectra of fresh and used 5%GO-$CoFe_2O_4$ samples. It was possible to deconvolute Co 2p into two peaks with binding energies (B.E.) of 780.9 and 778.6 eV, corresponding to Co^{II} and Co^{III}, respectively [43]. After oxidation, the content of Co^{II} increased from 46% to 52%, while the proportion of Co^{III} decreased by 6% (Fig. 9a). The peaks at higher B.E. (712.4 eV) in Fig. 9b were attributed to Fe^{III}, while lower B.E. (710.2 eV) were associated to Fe^{II} [44]. 54% and 46% of the total Fe was represented by the relative ratios of Fe^{II} and Fe^{III}, respectively. After reaction, the relative ratio of Fe^{II} dropped slightly, from 54% to 52%, correspondingly, Fe^{III} changed from 46% to 48%. The findings showed that the redox pairs of Co^{II}/Co^{III} and Fe^{II}/Fe^{III} played a role in the catalytic cycle, and aided in the conversion of charges to produce ROSs during PMS activation.

The O 1s spectra (Fig. 9c) was divided into three distinct peaks, which corresponded to H_2O at ~532.9 eV, adsorbed oxygen species (O_{ads}) at ~531.1 eV and lattice oxygen species (O_{latt}) at ~529.7 eV, respectively [45]. The quantity of O_{latt} was found to have decreased by 7% following the catalytic process, demonstrating that lattice oxygen was used during the catalytic reaction that went along with the redox of metal ions. Accordingly, the percentage of O_{ads} rose from 37% to 50%, showing that certain O_{ads} might change into O_{latt} by obtaining electrons from the system in conjunction with the oxidation of Co^{II} and Fe^{II}. Additionally, the role of dissolved O_2 was also be confirmed. As shown in Fig. S9 (Supporting information), the DBP degradation under N_2 condition almost equaled the one observed without gas introduction. Furthermore, there was also no visible discrepancy on ESR signal of TEMP-$^1O_2$ under air and N_2 atmosphere. Therefore, it indicated the dissolved O_2 in the water did not contribute significantly to the oxidation of DBP and the generation of $^1O_2$ in this system.

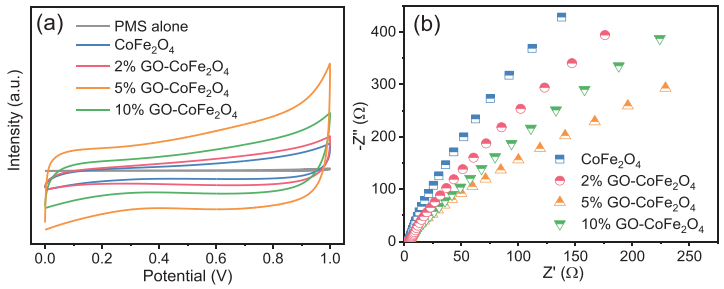

Fig. 7. (a) Cyclic voltammograms and (b) electrochemical impedance spectroscopy of different catalysts.

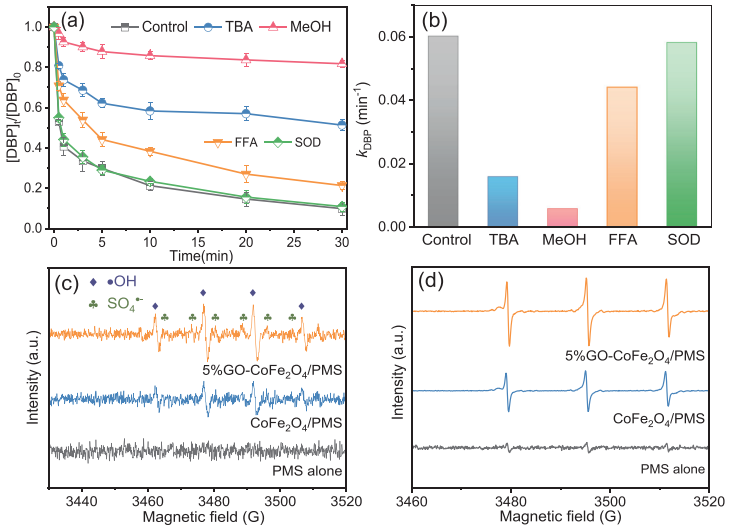

Fig. 8. Effect of different scavengers on (a) DBP degradation and (b) k constants in the 5%GO-$CoFe_2O_4$/PMS system. Spin-trapping ESR spectra for (c)$^{\bullet}OH/SO_4^{\bullet-}$ and (d) $^1O_2$ in the different PMS system. Catalysts: 0.1 g/L, $C_{0[DBP]}$: 2 μmol/L, $C_{[PMS]}$: 20 μmol/L, $C_{[TBA]} = C_{[MeOH]}$: 100 mmol/L, $C_{[FFA]}$: 1 mmol/L, $C_{[SOD]}$: 50 U/mL, initial pH of 7.0, T: 20 ± 2 °C.

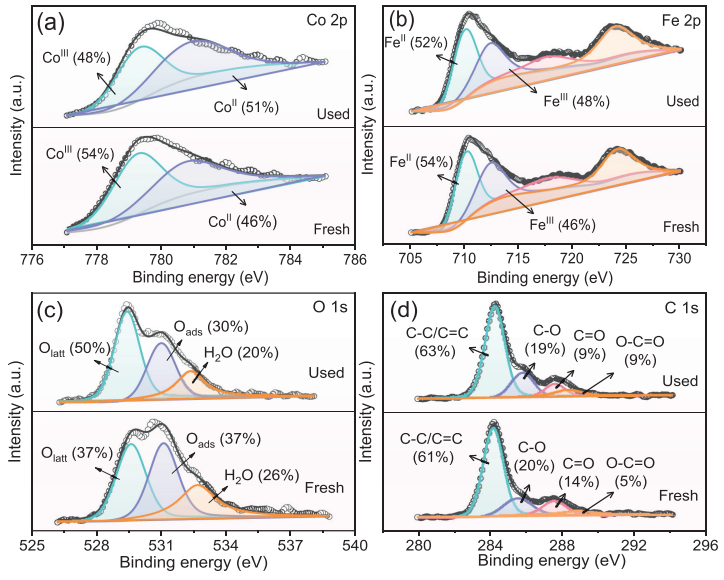

Fig. 9. XPS spectra of 5%GO-$CoFe_2O_4$: (a) Co 2p, (b) Fe 2p, (c) O 1s and (d) C 1s.

Furthermore, C–C/C=C, C–O, C=O, and O–C=O bonds were identified as the fitting peaks at 284.5, 286.2, 288.2, and 289.5 eV, respectively (Fig. 9d) [46]. After catalysis, it was discovered that the relative ratio of C=O in 5%GO-$CoFe_2O_4$ dropped from 14% to 9%. The study came to the conclusion that C=O took part in the catalytic reaction, and that the newly created $SO_4^{\bullet-}$ and $^{\bullet}OH$ were also capable of reducing the amount of C=O in 5%GO-$CoFe_2O_4$ through the radical oxidation process.

Based upon the aforementioned results, possible PMS activation pathways using GO-$CoFe_2O_4$ were postulated and schematically displayed in Fig. 10. DBP degradation was facilitated by both radical and non-radical routes in the GO-$CoFe_2O_4$/PMS system. HSO_5^- and Co^{II}/Fe^{II} on the surface of catalyst reacted to form $SO_4^{\bullet-}$, which then oxidized the Co^{II}/Fe^{II} to Co^{III}/Fe^{III} (Eq. 1). Simultaneously, Co^{III}/Fe^{III} reacted with HSO_5^- to produce $SO_5^{\bullet-}$ (Eq. 2), Additionally, H_2O or OH^- could partially react with $SO_4^{\bullet-}$ to gener-

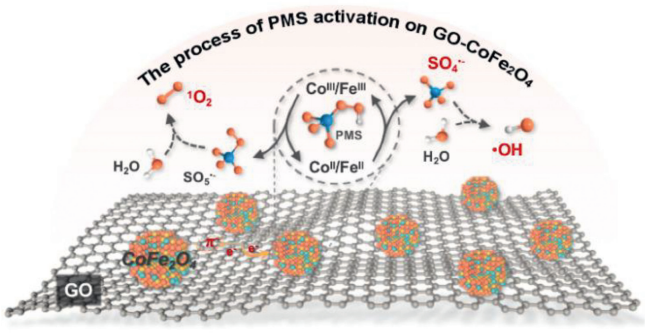

Fig. 10. Scheme of proposed mechanism of PMS activation on GO-$CoFe_2O_4$.

ate $^{\bullet}OH$ in part (Eq. 3). $^1O_2$ was created *via* the interaction between H_2O and $SO_5^{\bullet-}$ or the compound of $SO_5^{\bullet-}$ (Eqs. 4 and 5). During the GO-$CoFe_2O_4$/PMS process, the redox cycles of Fe^{III}/Fe^{II} and Co^{III}/Co^{II} improved the transport of electrons and the production of various ROSs. In the meantime, the plenty of oxygen-containing groups on the surface of GO, such as C=O groups, were electron-rich and hence had a significant potential to coordinate a redox process [47,48]. Additionally, free-flowing electrons from sp^2 hybridized carbon network with unpaired electrons promoted the formation of ROSs [49]. Finally, the DBP molecules were quickly broken down by the producing ROSs into minor organic intermediates or even CO_2 and H_2O (Eq. 6).

$$Co^{II}/Fe^{II} + HSO_5^- \rightarrow Co^{III}/Fe^{III} + SO_4^{\bullet-} + OH \quad (1)$$

$$Co^{III}/Fe^{III} + HSO_5^- \rightarrow Co^{II}/Fe^{II} + SO_5^{\bullet-} + H^+ \quad (2)$$

$$SO_4^{\bullet-} + H_2O \rightarrow SO_4^{2-} + {}^{\bullet}OH \quad (3)$$

$$2SO_5^{\bullet-} + H_2O \rightarrow 2HSO_4^{2-} + 1.5\,{}^1O_2 \quad (4)$$

$$SO_5^{\bullet-} + SO_5^{\bullet-} \rightarrow 2SO_4^{2-} + {}^1O_2 \quad (5)$$

$$SO_4^{\bullet-}/OH/{}^1O_2 + DBP \rightarrow \text{intermediates} + CO_2 + H_2O \quad (6)$$

In conclusion, a series of GO-$CoFe_2O_4$ catalysts with various GO loading levels were prepared. They showed enhanced catalytic activity compared to pure $CoFe_2O_4$ in activating PMS for DBP degradation. The excellent removal effectiveness of DBP was achieved under the optimal conditions of 0.1 g/L 5%GO-$CoFe_2O_4$, 20 μmol/L PMS, 2 μmol/L of DBP at an initial pH of 7.0, where the attained degradation of DBP was 90%. 5%GO-$CoFe_2O_4$ demonstrated a significant increase in catalytic function with the k_{DBP} value of 0.060 min^{-1}, which was almost three times greater than that of $CoFe_2O_4$ ($k_{DBP} = 0.015$ min^{-1}). Moreover, recyclability tests revealed that GO-$CoFe_2O_4$ was stable and reusable. The PMS utilization efficiency was significantly improved by the batch dosing of catalysts. Electrons cycling between Co^{II}/Co^{III} and Fe^{II}/Fe^{III} led to the cleavage of PMS to produce $SO_4^{\bullet-}$ and $^{\bullet}OH$ and $^1O_2$, which attacked DBP molecules to degrade into tiny molecular species and then further mineralized into CO_2 and H_2O. The synergistic function between $CoFe_2O_4$ and GO led to effective PMS activation and increased $SO_4^{\bullet-}$ and $^{\bullet}OH$ generation.

Declaration of competing interest

The authors declare no conflict of interest.

Acknowledgments

We appreciate the financial support of the National Natural Science Foundation of China (Nos. 52200010, 52000050), Postdoctoral Science Foundation of China (Nos. 2022M710954, 2020M670913), Open Project of State Key Laboratory of Urban Water Resource and Environment (Harbin Institute of Technology) (Nos. HC202240, 2021TS22).

Supplementary materials

Supplementary material associated with this article can be found, in the online version, at doi:10.1016/j.cclet.2023.108397.

References

[1] K. Fent, A.A. Weston, Aquat. Toxicol. 76 (2006) 122–159.
[2] O. Bajt, G. Mailhot, M. Bolte, Appl. Catal. B: Environ. 33 (2001) 239–248.
[3] B. Wang, H.X. Wang, W. Zhou, et al., Environ. Sci. Technol. 49 (2015) 1120–1129.
[4] J. Lee, U.V. Gunten, J.H. Kim, Environ. Sci. Technol. 54 (2020) 3064–3081.
[5] W.D. Oh, Z. Dong, T.T. Lim, Appl. Catal. B: Environ. 194 (2016) 169–201.
[6] J.L. Wang, S.Z. Wang, Chem. Eng. J. 334 (2018) 1502–1517.
[7] P.D. Hu, M.C. Long, Appl. Catal. B: Environ. 181 (2016) 103–117.
[8] J. Deng, Y. Shao, N. Gao, et al., J. Hazard. Mater. 262 (2013) 836–844.
[9] K. Zhang, D. Sun, C. Ma, et al., Chemosphere 241 (2020) 125021.
[10] Y.M. Ren, L.Q. Lin, J. Ma, et al., Appl. Catal. B: Environ. 165 (2015) 572–578.
[11] L.J. Xu, W. Chu, L. Gan, Chem. Eng. J. 263 (2015) 435–443.
[12] A.T. Smith, A.M. LaChance, S. Zeng, B. Liu, L. Sun, Nano Mater. Sci. 1 (2019) 31–47.
[13] J.P. Zhou, H.L. Liu, J. Luo, et al., ACS Appl. Mater. Interfaces 8 (2016) 18140–18149.
[14] Z.Q. Cai, A.D. Dwivedi, W.N. Lee, et al., Environ. Sci.-Nano 5 (2018) 27–47.
[15] L. Tang, X. Meng, D. Deng, X. Bao, Adv. Mater. 31 (2019) 1901996.
[16] W. Choi, I. Lahiri, R. Seelaboyina, Y.S. Kang, Crit. Rev. Solid State 35 (2010) 52–71.
[17] X. Zhu, Y. Zhu, S. Murali, M.D. Stoller, R.S. Ruoff, ACS Nano 5 (2011) 3333–3338.
[18] C. Chen, W. Cai, M. Long, et al., ACS Nano 4 (2010) 6425–6432.
[19] X.R. You, C.Y. Huang, W. Huang, et al., Environ. Sci.: Nano 7 (2020) 554–570.
[20] J. Deng, L.W. Xiao, S.J. Yuan, et al., Sep. Purif. Technol. 255 (2021) 117685.
[21] R. Tabit, O. Amadine, Y. Essamlali, et al., RSC Adv. 8 (2018) 1351–1360.
[22] W.S. Hung, S.M. Chang, R.L.G. Lecaros, et al., Carbon 117 (2017) 112–119.
[23] N. Meng, R.C.E. Priestley, Y. Zhang, H.T. Wang, X.W. Zhang, J. Membrane Sci. 501 (2016) 169–178.
[24] D.R. Yang, J. Feng, L.L. Jiang, et al., Adv. Funct. Mater. 25 (2015) 7080–7087.
[25] N. Li, Z.F. Geng, M.H. Cao, et al., Carbon 54 (2013) 124–132.
[26] M. Seredych, T.J. Bandosz, J. Mater. Chem. 22 (2012) 23525–23533.
[27] M. Kim, C. Lee, J. Jang, Adv. Funct. Mater. 24 (2014) 2489–2499.
[28] K. Ashwini, A.D. Mashkoor, S. Poorva, V. Dinesh, AIP Conf. Proc. 1148 (2014) 1148–1150.
[29] T. Lin, L. Yu, M. Sun, et al., Chem. Eng. J. 286 (2016) 114–121.
[30] Y. Zhao, H.Z. An, G.J. Dong, et al., App. Surf. Sci. 505 (2020) 144476.
[31] Y. Zhao, S. Wang, T. Wei, Y.M. Ren, T.Z. Luan, J. Environ. Chem. Eng. 10 (2022) 107241.
[32] J. Liu, Z.W. Zhao, P.H. Shao, F.Y. Cui, Chem. Eng. J. 262 (2015) 854–861.
[33] Z.L. Wu, Z.K. Xiong, R. Liu, et al., J. Hazard. Mater. 427 (2022) 128204.
[34] R.H. Zhang, M.L. Chen, Z.K. Xiong, Y. Guo, B. Lai, Chin. Chem. Lett. 33 (2022) 948–952.
[35] Z. Wang, R.T. Bush, L.A. Sullivan, C.C. Chen, J.S. Liu, Environ. Sci. Technol. 48 (2014) 3978–3985.
[36] S. Wang, M.Y. Zhang, J. Feng, et al., Chem. Eng. J. 430 (2022) 133175.
[37] Z. Liu, H. Ding, C. Zhao, et al., Water Res. 159 (2019) 111–121.
[38] Y. Zhao, H.Z. An, J. Feng, Y.M. Ren, J. Ma, Environ. Sci. Technol. 53 (2019) 4500–4510.
[39] Z.C. Yang, J.S. Qian, A.Q. Yu, B.C. Pan, Proc. Natl. Acad. Sci. U. S. A. 116 (2019) 6659–6664.
[40] E.T. Yun, J.H. Lee, J. Kim, H.D. Park, J. Lee, Environ. Sci. Technol. 52 (2018) 7032–7042.
[41] J.J. You, C.Y. Zhang, Z.L. Wu, et al., Chem. Eng. J. 415 (2021) 128890.
[42] J.E. Yang, Y. Lin, H.H. Peng, et al., Appl. Catal. B: Environ. 268 (2020) 118549.
[43] L.P. Wu, B. Li, Y. Li, et al., ACS Catal. 11 (2021) 5532–5543.
[44] A.H. Mady, M.L. Baynosa, D. Tuma, J.J. Shim, Appl. Catal. B: Environ. 244 (2019) 946–956.
[45] X.B. Hu, B.Z. Liu, Y.H. Deng, et al., Appl. Catal. B: Environ. 107 (2011) 274–283.
[46] X.T. Li, J. Wang, X.G. Duan, et al., ACS Catal. 11 (2021) 4848–4861.
[47] C. Liu, S. Liu, L. Liu, et al., Chem. Eng. J. 379 (2020) 122274.
[48] L.Y. Wu, Z.Y. Li, P.T. Cheng, et al., Water Res. 223 (2022) 119013.
[49] J. Ye, J.D. Dai, D.Y. Yang, C.X. Li, Y.S. Yan, J. Environ. Chem. Eng. 9 (2021) 106076.